J Therm Spray Tech (2025) 34:2256–2266
https://doi.org/10.1007/s11666-025-02011-6

ORIGINAL RESEARCH ARTICLE

Effect of Process Parameters on Residual Stresses of Cold Gas Sprayed IN718 Coatings on Large Repair Geometries

J.-C. Schmitt[1] · F. Lang[2] · J. Fiebig[1] · T. Sievert[1] · J. Gibmeier[2] · O. Guillon[1,3] · R. Vaßen[1,4]

Submitted: 26 September 2024 / in revised form: 1 April 2025 / Accepted: 24 April 2025 / Published online: 28 May 2025

Abstract The residual stresses induced by the various process conditions in engineering components can have a significant impact on their structural integrity and performance. It is essential to ensure reliable control of the mechanical properties of structural components during the repair process, as this directly affects their performance and longevity. Cold gas spray, a solid-state deposition technique, involves the high-velocity impact of fine powder particles onto a substrate, resulting in the formation of a dense, metallurgically bonded coating. The aim of this study is to investigate the suitability of cold gas spraying parameters for the repair of large cavities in components made of Inconel 718. Two sets of parameters, approaching the limits of the spraying facility, have been utilized and analyzed using particle diagnostics. Experimental methodologies involve the characterization of residual stress profiles using techniques such as in situ curvature measurement and the incremental hole drilling method after the cold gas spray repair. Additionally, the microstructure and topography of the as-sprayed repair coatings are demonstrated. The results demonstrate the ability of cold gas spray to successfully fill deep repair cavities and adjust the residual stress state of such repair coatings by varying the processing parameters. Lower residual compressive stresses in the layer were achieved by utilizing gas parameters, wherein the particles impact the substrate at an elevated temperature and at a comparatively reduced velocity. Both conditions exhibited coatings with consistent microstructure, good adhesion and uniform topography without major defects. This research demonstrates the potential of cold gas spray as a viable and efficient repair method for large repair geometries, offering a promising avenue for enhancing the reliability and lifespan of critical engineering structures.

Keywords feedstock, residual stress · inconel · processing, cold spray · processing, repair · properties, diagnostics

Abbreviations

CGS	Cold gas spray
CSM	Cold spray meter
DE	Deposition efficiency
ICP	In-situ coating properties sensor
IN718	Inconel 718

Variables

d [µM]	Particle diameter
d_{50} [µM]	Particle mean size diameter
E'_s [MPa]	Biaxial Young's modulus, substrate
L_{dep} [Mm]	Spray distance
$p_{g,init}$ [MPa]	Process (Initial) pressure
p [MPa]	Pressure
T [°C]	Temperature
$T_{g,init}$ [°C]	Process (Initial) gas temperature
T_s [°C]	Substrate temperature
T_{pre} [°C]	Temperature during pre-heating

✉ J.-C. Schmitt
jo.schmitt@fz-juelich.de

[1] Materials Synthesis and Processing (IMD-2), Forschungszentrum Jülich GmbH, Institute of Energy and Climate Research, 52425 Jülich, Germany

[2] Institut für Angewandte Materialien (IAM-WK), Karlsruhe Institute of Technology (KIT), Kaiserstraße 12, D-76131 Karlsruhe, Germany

[3] Jülich Aachen Research Alliance: JARA-Energy, 52425 Jülich, Germany

[4] Institut für Werkstoffe, Ruhr-Universität Bochum, Bochum, Germany

T_{av} [°C]	Average surface temperature
t_c [Mm]	Thickness, coating
t_s [Mm]	Thickness, substrate
v [M s^{-1}]	Velocity
v_R [M s^{-1}]	Robot scanning speed
z_{dep}	Number of deposition cycles
x, y, z	Spatial coordinates
α	Spray angle
κ [M^{-1}]	Curvature
σ_{RS} [MPa]	Residual stress
$\varnothing_{mill}$ [Mm]	Diameter of the end mill

General Subscripts

xx	X-direction
yy	Y-direction
1	Condition 1
2	Condition 2
g	Gas
p	Particle
s	Substrate
c	Coating

Introduction

Cold gas spray (CGS) technology has emerged as a fast and inexpensive method for repairing components, where several millimeters thick layers can be deposited quickly. Cold gas spray applications extend across various industries, ranging from aerospace and automotive to oil and gas, where the demand for efficient and cost-effective repair solutions is paramount (Ref 1-4). CGS offers a unique set of advantages in comparison with conventional repair techniques. The process utilizes solid particles, mostly in the form of metal powders and accelerated to supersonic speed (300 m/s-1200 m/s). Typically, the use of nitrogen as a process gas within a de Laval nozzle directed toward a substrate for the purpose of coating deposition is achieved without the necessity for extensive heat input upon reaching a sufficient speed, the so-called critical velocity. At this point, the particles undergo significant plastic deformation, resulting in the formation of a dense and cohesive coating (Ref 5-8). Unlike conventional thermal spray techniques, CGS operates at temperatures below the melting point of the sprayed material, minimizing thermal degradation and preserving the intrinsic properties of the deposited material. CGS is therefore recognized as a repair technology in addition to conventional technologies such as welding or laser processing (Ref 9-12) but also in the scope of additive manufacturing (Ref 13-15).

In the realm of analysis methods, understanding the characteristics of CGS coatings is crucial for optimizing performance and ensuring the longevity of repaired components. Residual stresses, important to asses in the structural integrity of coatings, is a focus of investigation in cold gas spray applications. The residual stress state in thermally sprayed coatings can be attributed to three origins. Peening stresses are induced due to the impact of solid particles on the substrate surface, which are compressive in nature (Ref 16). Quenching stresses result from the cooling of hot particles, typically in a molten state, on a cold substrate, creating tensile stresses. After the deposition, thermal stresses evolve due to the mismatch between the coefficient of thermal expansion for coating and substrate, which can manifest as compressive or tensile stresses depending on that mismatch (Ref 17). Due to the dominant peening effect of impacting solid particles and the relative low thermal effect, the overall residual stress state in cold gas spray is often compressive (Ref 18, 19). Compressive residual stresses can accelerate the failure of the layers at high layer thicknesses (Ref 20). It is, therefore, essential to gain knowledge of the residual stresses, especially for more extensive repairs. Frequently, the incremental hole drilling method was applied to obtain the through-thickness stress states in CGS coatings, indicating the in-depth stress profiles up to a limited thickness (Ref 19, 20). The utilization of advanced techniques, such as neutron diffraction, which possesses the capacity to penetrate dense materials and provide non-destructive three-dimensional stress mappings, has become an integral component in the evaluation of the structural integrity of cold-sprayed coatings. However, these analyses need access to large scale facilities and the applicability is severely limited due to the limited accessibility of measurement options (Ref 21, 22). Another technique that is widely utilized for the measurement of residual stresses in materials and thin films is the curvature method. This method involves determining the deformation—or curvature—induced in a substrate as a consequence of the presence of residual stresses. By analyzing the curvature of the substrate, which can be obtained using techniques such as optical profilometry, the residual stresses can be quantified. The curvature method is non-destructive and applicable to a variety of material systems and film thicknesses. The fundamental principle is based on the Stoney formula, which relates the curvature of the substrate to the stress in the coating connects the stress values to the curvature data (Ref 23). In thermal spray, such experiments based on the curvature method have typically been carried out by utilizing the In Situ Coating Properties (ICP) sensor. As this device measures the displacement of the specimen during the subsequent spraying cycles, it can provide valuable insights into deposition characteristics, e.g., curvature or cracking. A number of authors have employed the in situ curvature method in CGS on a diverse range of materials (Ref 16, 24-26).

The developing residual stress state is mainly set by the characteristic deposition. Particle in-flight diagnostics in CGS enable the prediction of deposition characteristics, especially regarding critical conditions necessary for successful bonding. The coating properties are mainly determined by particle velocity and temperature. The latter is hard to measure due to the particles' low temperature and high velocity. In literature, a high-speed infrared camera has been utilized to determine the particle temperature (Ref 27, 28). For measuring the particle velocity, several studies demonstrated a reliable measurement, typically applying a DPV-type device such as the cold spray meter (CSM) (Ref 29, 30) or a camera-based device like the HiWatch system (Ref 31).

This study focused on the deposition of Inconel 718 (IN718) powder onto IN718 substrates, a nickel-based superalloy that is frequently used for high-temperature components in gas turbines. In a previous study by Lang et al. (Ref 21), two normalized sets of parameters were investigated for a suitable repair process for significant defects. To assess the quality of the repair, the microstructure and residual stress distribution were analyzed on the cross section of a repaired cavity. In addition to the non-destructive neutron diffraction analyses applied in the referred study, residual stress depth distributions were complementary analyzed using the incremental hole drilling method and the in situ curvature measurement. In-flight diagnostics were conducted during the spray process to investigate the article properties. The study aims to improve the understanding of the interaction between the processing gas parameter and the utilized particles, as well as their influence on the evolving residual stress state of the cold gas sprayed coatings and the repair geometry dimensions.

Experimental Methods

Sample Preparation

IN718-powder (Oerlikon-Metco, Troy, MI, USA) with spherical morphology (d_{10} = 9.5 µm, d_{50} = 14 µm, d_{90} = 20 µm) has been used as coating material (Ref 32). As substrate material, solution heat treated IN718-plates (100 mm × 50 mm × 12 mm) with a centered cavity (50 mm × 20 mm × 4 mm) have been used. Since these are the main subjects of this study the geometries will be called 'cavity' from here on. The repair geometry employed corresponds to the anticipated configuration of a milled-out cavity, resulting from the repair process. As illustrated in Figure 1, the sidewalls of the cavity are tapered with an angle of 60° in order to improve gas flow during cold gas spraying with respect to the bow shock effect (Ref 33). Such a wall angle provides a sufficiently small deviation from the optimum impact angle of the particles to ensure a well-adhering coating. A more detailed view is given in Lang et al. (Ref 21). Due to the milling process, the hardness in the near surface region affected by the machining locally increased compared to the softer substrate material. No further surface treatment has been applied.

An Impact 5/11 system (Impact Innovations GmbH, Rattenkirchen, Germany) with a water-cooled D24 De Laval-Type converging-diverging nozzle was used for the deposition of the powder. To fill up the 4 mm deep cavity, 46 passes (z_{dep}) have been used at a spraying distance (L_{dep}) of 60 mm, a spraying angle of 90° (α_{dep}) and a robot scanning speed of 500 mm/s (v_R). The spray meander corresponds to the length of the long edge of the substrate with 1 mm vertical spacing for a total of 20 line profiles. Before deposition, three pre-heating cycles in terms of moving the nozzle without inserting any powder have been applied to increase the substrate adhesion (Ref 34).

Focusing on the influence of processing conditions of the process gas (N_2), two conditions were the subject of this study. A gas temperature of 950 °C ($T_{g,init}$) and a gas pressure of 4 MPa ($p_{g,init}$) have been extensively investigated in previous publications (Ref 19, 20, 26). Here, the objective was to achieve higher gas temperatures at a comparatively lower gas pressure and thus gas velocity. With standard, pressure-controlled operation of the gun, the pressure increases proportionally to the temperature increase. With flow-controlled operation, however, this increase can be smaller. Temperature and pressure shifted to 1050 °C and 4.5 MPa have been applied with the aim of obtaining low-velocity, hot particles for decreasing the peening effect and therefore reducing the standard compressive residual stresses in CGS (Ref 21). A summary of the conditions is given in Table 1. For each spray run, the temperature was captured using a pyrometer type 3MH1 (Optris GmbH, Berlin, Germany) with ε = 0.6, focused on the center of the substrate / cavity ground.

Characterization Methods

Thickness measurements of as-delivered and as-sprayed specimens were performed using a micrometer screw and topographical analysis using an optical profilometer with a P-CHR-10000 sensor (Model CT350T, cyberTECHNOLOGIES GmbH, Eching-Dietersheim, Germany). The latter was also used for roughness measurements with a CHR-1000 sensor inside of the cavity surface limited by the surplus material. Each specimen has been weighted before and after the deposition for the evaluation of the deposition efficiency (DE), which is the ratio of the total material sprayed to the material that was actually deposited.

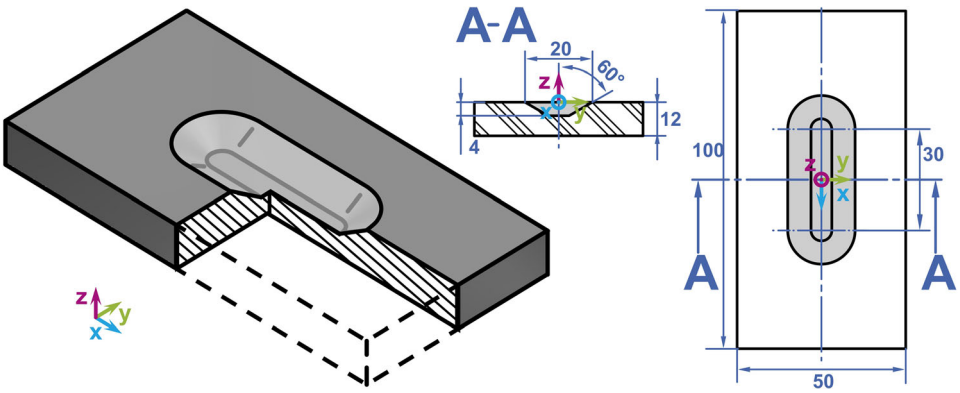

Fig. 1 3D rendering and technical drawing of the sample geometry with the cavity induced by machining and indication of the used specimen coordinate system. All dimensions are given in mm

Table 1 Spraying conditions applied in the present study

Condition	Name	$T_{g,init}$, °C	$p_{g,init}$, MPa	L_{dep} , mm	z_{dep} -	v_R ,mm s^{-1}
1	Standard	950	4.0	60	46	500
2	Hot	1050	4.5	60	46	500

Vickers microhardness testing (HV0.1) was conducted in accordance with the specifications outlined in DIN EN ISO 6507-1 (Ref 35), utilizing a Q10 A + instrument (ATM Qness GmbH, Golling an der Salzach, Austria). For microhardness testing, samples were cut according to the A-A reference in Figure 1 using electrical discharge machining (EDM). Furthermore, the samples were embedded in two-component universal embedding resin VariKEM 200 (Schmitz Metallographie GmbH, Herzogenrath, Germany). The specimens were ground, polished, and subsequently fine polished using an oxide polishing suspension (OPS). A total of 1479 indentations were arranged in a 12.5 × 7 mm^2 grid, extending from the center of the cavity into the surrounding substrate. The distance between the indentations is y = z = 250 µm.

For microstructural investigation, the remaining cut copy was ground and polished until the final SiO_2 suspension at the ATM Saphir 550 (Struers GmbH, Willich, Germany). The cross section has been investigated with a tabletop scanning electron microscope EM-30N (coXem, Daejeon, Republic of Korea) using a backscattered electron (BSE) detector. Additional EDS data has been obtained by applying a scanning electron microscope type EVO 15 (Zeiss, Oberkochen, Germany) using an EDS detector (ULTIM MAX 100, OXFORD INSTRUMENTS). Porosity has been by means of image analysis using the software ImageJ (Ref 36) evaluating seven SEM-Images at the same magnification.

A HiWatch HR2 system (Oseir Ltd., Tampere, Finland) has been applied for in-flight particle diagnostics. This high-resolution spray diagnostic instrument uses a pulsed diode laser as a light source to analyze the particle plume within a gauge volume. Contours of the particles are obtained by localized extinction of the uniform laser field in a high-resolution camera on the opposite side. The setup is described more detailed by Koivuluoto et al. (Ref 37).

Residual Stress Analysis

Residual stress depth profiles near the surface of the filled cavity in the as-sprayed condition were obtained by means of the incremental hole drilling method (Ref 38-40). Therein a blind hole is drilled incrementally into the material. The material removal causes the redistribution of residual stresses around the hole and results in strain relaxation that can be measured using strain gauges placed at fixed angles on the surface around the blind hole. Using calibration data and material specific elastic constants, in-plane residual stresses can be calculated from the measured strain relaxations.

A RS-200 Residual Stress Milling Guide and strain gauge rosettes of type EA-06-031-120 (ASTM Type A, (Ref 41), both from Micro-Measurements, Raleigh, NC, USA, were used to drill and measure the resulting strain relaxations, respectively. Incremental hole drilling analyses were conducted in the center of the cavity in the as-sprayed condition for both conditions using TiN coated carbide end mills with a diameter of $\varnothing_{mill}$ = 0.8 mm. Prior to application of the strain gauge rosettes, the measurement location had to be carefully machined, to create a smooth and level surface, i.e., the surplus material was removed and the surface roughness after CGS was reduced. The residual stress calculation was carried out using the differential approach (Ref 42), using bulk values for Nickel with the elastic constants E = 204 GPa and ν = 0.299 according to Kröner (Ref 43), based on single crystal coefficients determined in Dye et al. (Ref 44).

Furthermore, the residual stress state was evaluated on reference samples utilizing the ICP sensor (Reliacoat Technologies LCC, East Setauket, USA). For this sensor, geometries with dimensions of 228.0 mm x 25.4 mm x 3.0 mm have been employed. This device incorporates thermocouples on the back side of the sample to measure the substrate temperature, in addition to front side measurements via a pyrometer. The displacement is captured via three lasers and simultaneously transferred into the corresponding curvature. The complete setup is described in detail elsewhere (Ref 26, 45). The curvature can be back-calculated into the related residual stresses by employing the well-known Stoney equation (Eq. 1), assuming a uniform stress state of the coating (Ref 23):

$$\sigma_{RS} = \frac{E'_s t_s^2}{6 t_c} \kappa \qquad \text{(Eq 1)}$$

where σ_{RS} is the calculated residual stress, κ is the evolving curvature over the deposition process equal to the inverse curvature radius R. E'_s, t_s, and t_c are the substrates biaxial Young's modulus ($E' = E/(1\text{-}\nu)$) and thickness of substrate and coating, respectively. The applied material data are given in Table 2.

Results and Discussion

Coating Properties of the As-Sprayed Specimen

A photograph of the resulting topography profile of the cavities after 46 deposition cycles is displayed in Figure 2(a). The circular-shaped cavity ground (see Figure 1) has been subsequently reproduced until the end of the deposition process. Compared to the 4 mm deep cavities, slopes from surplus material have been built up at an appropriate size. A non-homogeneous coating surface within the cavity and on top of the surplus material is visible. Since there is a specific deviation of the deposition efficiency (DE) per spraying pass, depending on the particular impact angle, this might ascendingly derivate during the subsequent deposition cycles and result in a non-uniform shape. A slight, sharp slope was observed at the top of the cavity. This slope is constrained by the 60° flank and the endpoint of the continuous spray meander.

Table 2 Young's modulus, Poisson ratio and thickness of the utilized IN718 substrate material (Ref 26)

Material	E, GPa	ν, -	t_s, mm
IN718 substrate	200	0.29	3.2

The contour of the profile from conditions 1 and 2 is illustrated in Figure 2(b) and (c), respectively. The non-coated sample surface was employed as a reference point (height = 0 mm). Both cavities have been filled with repair material to a consistent topography and similar height. As observed in the as-sprayed state, the inner surface of the cavity exhibited non-uniformity. Topographical analyses revealed a slight negative offset at the dark blue areas where the repair material occasionally did not sufficiently fill the cavity. To ensure sufficient height for both conditions, it was determined that more passes were necessary. The non-flat surface led to a roughness of approximately $R_{a,cond1} \approx 7.9 \pm 0.3$ µm and $R_{a,cond2} \approx 7.3 \pm 0.2$ µm. As the 4 mm deep cavity was filled with 4 mm of repair material, the surplus material at the long edge behind the cavity reached the same height. A slight increase in height was observed for condition 2, where the slopes revealed to be approximately 100 µm higher compared to condition 1. It can be observed that the build-up angle of the surplus material, as well as that of the slopes, has been reproduced in accordance with the 60° tapered wall angle of the cavity. In contrast, the regions exhibiting a dark blue coloration within the cavity are more prominent. As previously stated, statistical deviation per spray pass might arise, which increases in proportion to the number of deposition cycles. Furthermore, L_{dep} was observed to decrease with each subsequent deposition pass, which in turn influences the DE in general. This phenomenon is especially evident in the context of cavities and surfaces. In fact, the presence of a cavity can even increase the gas stagnation zone, since the gas is impeded from being evacuated from within the cavity. A more significant bow shock effect was assumed for condition 2 due to the increased gas pressure. Nevertheless, the DE for condition 1 was 73%, and for condition 2, it was 74%. Given that the overall topography, DE, and roughness are consistent for a well-filled cavity across both conditions, the bow shock effect was not identified as a critical issue in the actual study.

The surface temperature, measured via the pyrometer focused on the center of the cavity, is presented in Figure 3(a). 150 °C marks the lowest measuring threshold of the device. Each peak represents one deposition cycle up to the total number of 46. The three pre-heating cycles at the beginning for both conditions revealed a slight temperature increase in $T_{pre,1} \approx 210$ °C and $T_{pre,2} \approx 240$ °C. By adding a particle loading, the temperature of the subsequent cycles was further increased until a specific plateau for each condition was reached. As anticipated, the elevated processing gas temperature resulted in a higher average temperature magnitude during deposition for condition 2 ($T_{av,2} \approx 360$ °C) in comparison with condition 1 ($T_{av,1} \approx 320$ °C). In comparison with previous studies on cold gas sprayed IN718 on flat substrates utilizing

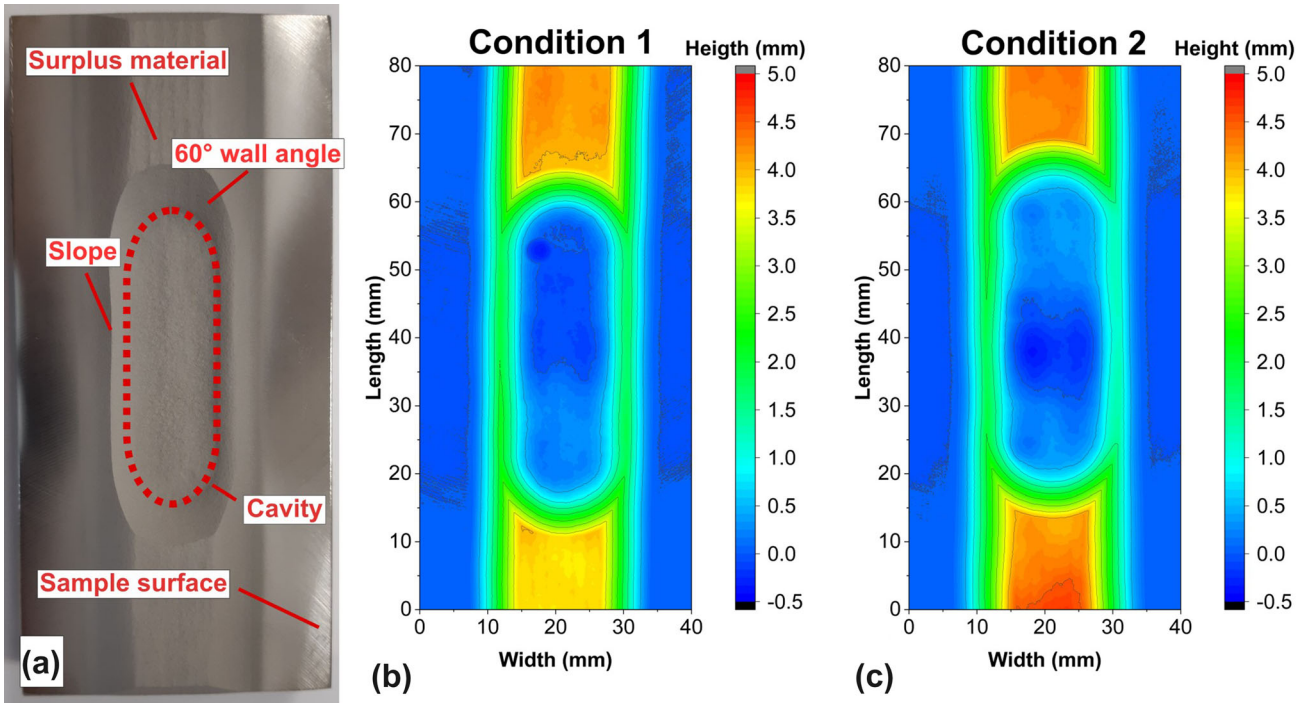

Fig. 2 Topography of the as-sprayed cavities is displayed in representative form for condition 1 (a). A two-dimensional contour map of the topography after CGS is provided for conditions 1 (b) and 2 (c)

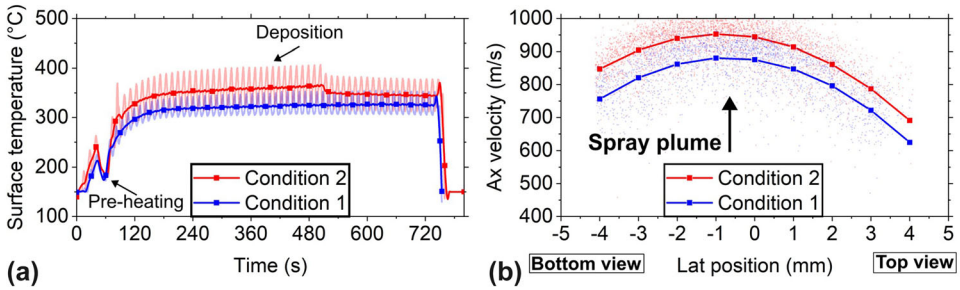

Fig. 3 Temperature during spraying has been obtained for both conditions (1 = blue, 2 = red) by utilizing a pyrometer (a) focused on the center of the sample. The particle velocity for each condition has been measured via HiWatch System (b). Both the temperature and velocity have been fitted for improved readability. The raw data is presented in a transparent format (Color figure online)

condition 1 (Ref 26), the average surface temperature is approximately 40 °C higher.

The particle velocity as measured via HiWatch was found to be marginally higher for condition 2 (illustrated in Figure 3b) with the maximum magnitude occurring at-1 mm ($v_{max,1}$ = 880 m/s < $v_{max,2}$ = 952 m/s). The present study considers only the lateral position, with a distance of 4 to-4 mm covered by the HiWatch system, which captures the entire particle plume. The fitted velocity profile exhibited a consistent shape for both conditions, with the highest velocity observed in the center and the lowest velocity at the edges of the spray plume. The elevated particle velocity observed in condition 2 can be attributed to the increased processing gas pressure, which consequently resulted in a higher gas velocity.

In order to investigate the original postulated thesis concerning particles that are both hotter and slower, the ratio of the average surface temperature and the maximum particle velocity for both conditions has been verified. The (surface) temperature for condition 2 is approximately 13% higher. Conversely, the particle velocity has only increased by approximately 7, 6%. It is evident that further analysis and interpretation of the statistical data is required. Additionally, alterations may be necessary due to the lateral position shift of the particle measurement and the fact that the temperature is only recorded at a single point. Nevertheless, the data can provide insight into how the processing conditions have influenced the particle characteristics.

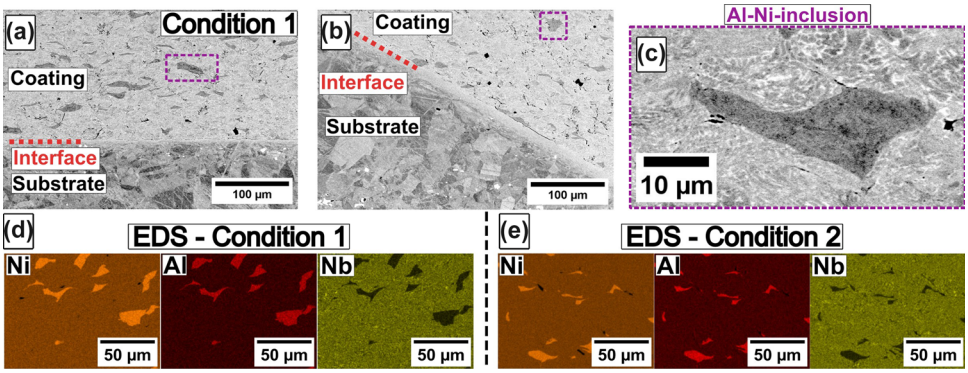

Fig. 4 BSE-SEM micrographs demonstrate the interface at the cavity ground (a) and the tapered wall area (b) for condition 1. The microstructure can be considered representative of both conditions, also regarding the characteristic Al-Ni inclusions (c). SEM-EDS analyses have been conducted for Ni, Al and Nb on both conditions (d and e)

Microstructure and Hardness of the As-Sprayed Specimens

The findings in the microstructure are presented as an illustrative example in Figure 4 for both conditions under examination in relation to condition 1. No significant differences were identified in comparison with condition 2. In both cases, the coating consists of deformed particles at a low porosity level ($< 2\%$). In regard to the interface, it was observed that the coating exhibited satisfactory adhesion in both conditions, demonstrating no signs of delamination or separation from the substrate surface (Figure 4a). This phenomenon was also observed at the sidewalls. A deformation zone consisting of many small grains due to the peening effect is visible at the interface to the same extent for both conditions (Figure 4b). The illustrated interfacial area at the cavity ground is in good agreement to the findings observed for the sidewalls. The coating regime includes the powder characteristic Al-rich-Ni-inclusions scattered within the deformed particles and a grain structure in the substrate, also for both conditions (see Figure 4c). This is in good agreement with other studies using the same materials (Ref 19, 32). In general, the microstructure did not reveal any significant differences at the interface, within the cavity or the boundary of the surplus material for both conditions. Additionally, EDS analyses were conducted on the principal elements for the chosen Inconel 718 powder (Ref 32). Corresponding element distribution maps (Figure 4d and e) clearly reveal the presence of Al-rich-Ni-inclusions for both conditions. Those inclusions are surrounded by bright contrast areas enriched by Nb, which are assumed to be remains of the interdendritic areas that were formerly present in the particles (Ref 19).

Figure 5 depicts contour plots of Vickers microhardness (HV0.1) distribution on the cross section of conditions 1 (Fig. 5a) and 2 (Fig. 5b), respectively. The dashed, red lines represent the shape of the cavity (see A-A reference in Fig. 1), and the cross-hatched areas represent the specimens. The measurement positions are indicated by black dots. The results for condition 2 (Fig. 5b) are mirrored in the y-direction for visualization purposes. The results demonstrate comparable hardness values for both conditions with an average of approximately 502 ± 33 HV0.1 in the filled process zone and an average of approximately 226 ± 12 HV0.1 in the surrounding substrate. The hardness distribution for both conditions is almost homogeneous, despite the high spatial resolution and the rather small indentation size. As the powder particles do not contain precipitates, the observed increase in hardness within the filled process zone can be attributed to work hardening, which is a consequence of the strong plastic deformation.

Residual Stress Analysis of Both Conditions

Figure 6 illustrates the incremental hole drilling results in the center of the filled cavity for condition 1 and condition 2 both in the as-sprayed and machined states. Herein, condition 1 is displayed in blue and condition 2 in red, respectively. The results demonstrate the presence of compressive residual stresses in the x and y directions, represented by filled and unfilled symbols, respectively. The maximum principal stresses ($\sigma_{xx,max,1} \approx -200$ MPa, $\sigma_{yy,max,1} \approx -475$ MPa, $\sigma_{xx,max,2} \approx -75$ MPa and $\sigma_{yy,max,2} \approx -475$ MPa) are located in close proximity to the milled surface of the filled process zone and decrease with increasing depth. The accuracy of the residual stress analysis by means of incremental hole drilling for the nickel base alloy is estimated to be around 20-30 MPa. In contrast to the results for thin coatings on planar surfaces by Vaßen et al. (Ref 19), the residual stresses are direction-dependent with lower compressive residual stresses in the x-direction ($275 \text{ MPa} \leq \Delta\sigma_{xx-yy,2} \leq 75$ MPa and $400 \text{ MPa} \leq \Delta\sigma_{xx-yy,2} \leq 175$ MPa). These findings are in accordance with the results obtained through neutron diffraction residual stress mappings in the center of the cavities performed on similar samples (Ref 21). This may be attributed to the more substantial geometric constraints in the y-direction, namely the length of the cavity compared to the width. Such constraints could also result in different temperature gradients in each direction. Although

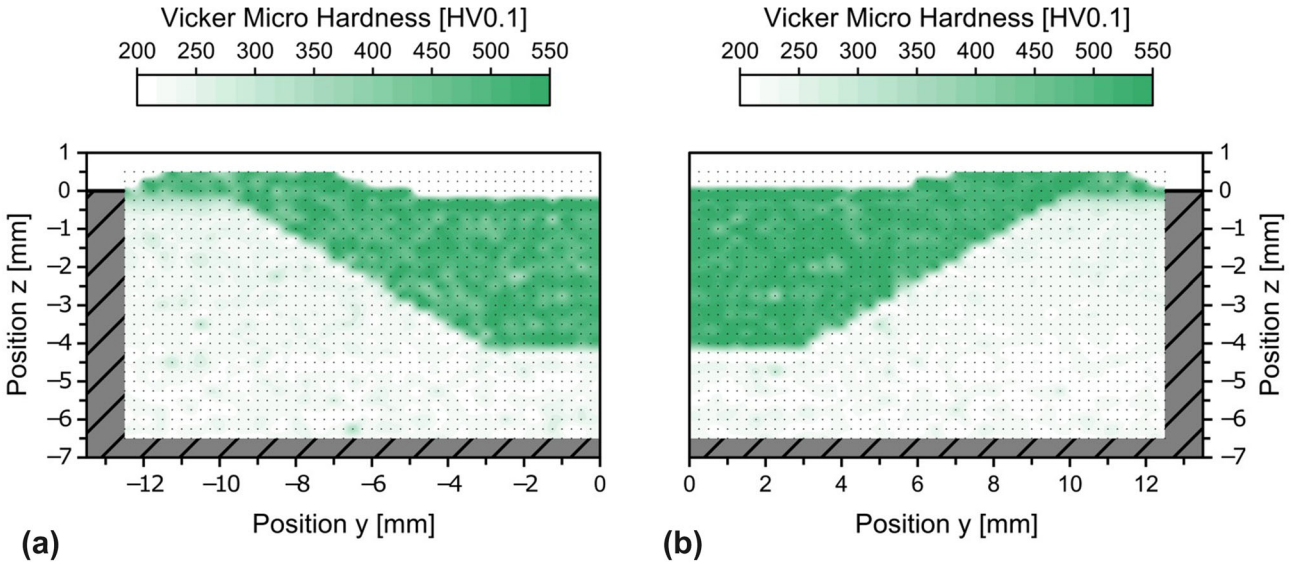

Fig. 5 Results for condition 1 (a) and condition 2 (b): Contour plots of the Vickers micro hardness mappings. The cross-hatched areas represent the specimen. The dashed lines represent the shape of the cavities. The black dots represent measurement locations. The results for condition 2 are mirrored for visualization purposes

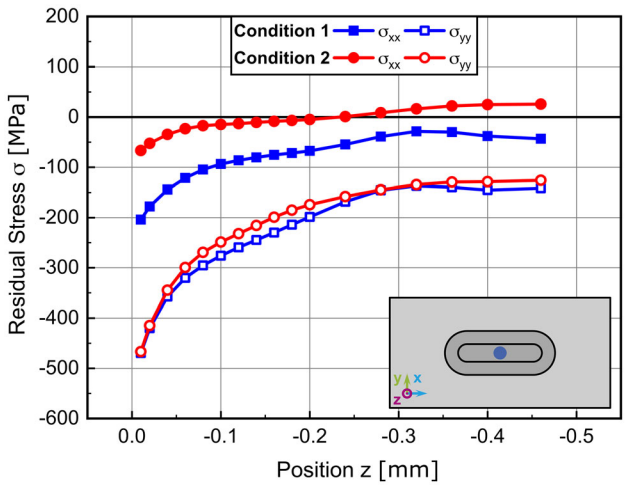

Fig. 6 Residual stress depth profiles obtained by means of incremental hole drilling for condition 1 (blue) and condition 2 (red) in the center of the cavities filled by means of cold gas spraying in x-direction (filled symbols) and y-direction (unfilled symbols) (Color figure online)

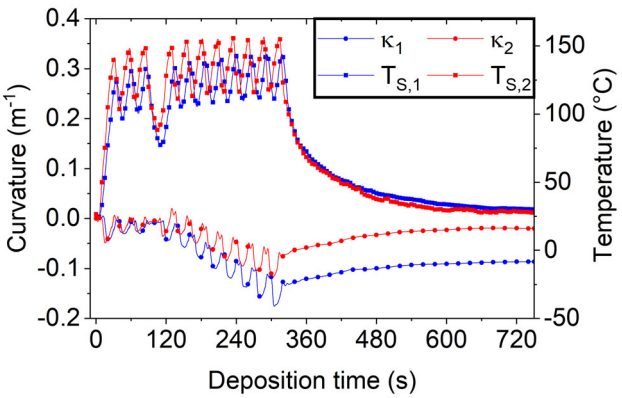

Fig. 7 Smoothed in situ curvature for condition 1 (blue circles) and condition 2 (red circles). Both conditions revealed a negative increase in curvature during deposition with a similar trend in curvature during the cooling period toward room temperature. A slightly elevated temperature at the substrate rear side could be observed for condition 2 (red squares) in comparison with condition 1 (blue squares) (Color figure online)

the residual stress courses for both samples are almost similar, condition 2 exhibits lower compressive residual stresses in the x-direction compared to condition 1. The difference between the initial and the final measurement points in residual stress decreases from $\Delta\sigma_{xx} \approx 125$MPa to $\Delta\sigma_{xx} \approx 75$MPa. This may be attributed to the larger heat input and subsequent relaxation in the sample repaired using the parameters for condition 2, as the gas temperature is higher (see Table 1). In contrast to the effects of hardness and microstructure, the choice of spraying parameters appears to affect residual stresses in repair fillings.

The results of the in situ curvature measurements on the 3 mm thick IN718 substrates are presented in Fig. 7 for both conditions. A negative increase in curvature, indicating compressive residual stresses, was evident after eight deposition cycles (starting from 120 s to 320 s) in both experiments. No initial curvature was observed after the first particle impact, and neither did a permanent curvature result from the pre-heating (Ref 26, 46). The curvature trajectory during the cooling period was found to be consistent across both conditions due to the similarity in material properties. In agreement with the findings from the DE of the cavity samples, the coating thickness was

similar, slightly above 700 µm. The measured temperature at the substrate rear side was observed to be increased for condition 2, in accordance with the conditions in Table 1.

During the cooling period, a uniform curvature change can be observed with respect to the shifted initial level of deposition curvature starting at 320 s. It is therefore assumed that the thermal stress is approximately equal for both conditions due to the equal material for substrate and coating, even for the elevated temperature. In combination with the less pronounced change in curvature, the overall amount of compressive stresses (deposition stress + thermal stress) is decreased for condition 2. This result agrees with the findings from the incremental hole drilling method as well as diagnostics of surface temperature and particle velocity. All data were summarized accordingly in Table 3. It is important to note that the curvature measurement results in a uniform stress distribution over the specimen, which does not account for the geometric constraints of the cavity. However, the ICP analysis is excellently suited to assess differences of the effect of changes in the processing parameters on the evolving stresses during the coating process.

The lower magnitude of negative curvature change may be related to a decreased peening effect in condition 2. Those particles yield an increased temperature level at the impact zone and can easier undergo shear deformation, which reduces the peening effect due to solid particle impact. As reported in the literature (Ref 24, 26), a thermal gradient can arise in cold-sprayed coatings. Such a thermal gradient is attributed to the heat input from gas and particles at the local gas spot. Upon the movement of the gas spot, the thermal gradient between the local temperature and the substrate temperature is balanced. The hereby arising residual stresses are tensile in nature, comparable to the quenching effect of molten splats in plasma spray processes. Such a thermal gradient has been analytically modeled by considering the heat balance at the impact zone (Ref 26). Condition 2 employs an increased processing temperature of the gas, rather than a longer gas spot residence time due to a slow robot traverse speed. It is assumed that both of these mechanics yield a comparable outcome in terms of an increased thermal gradient at the impact zone, which can compensate the dominant compressive residual stresses to a larger extend.

Table 3 Results of temperature (Pyrometer T_{av} and ICP sensor T_s), residual stress (ICP sensor σ_{RS}) and the maximum particle velocity (HiWatch v_p) for conditions 1 and 2

Condition	σ_{RS}, MPa	T_{av}, °C	T_S °C	v_p, m/s
1	− 50	320	125	880
2	− 10	360	135	952

The residual stress is calculated using the Stoney equation.

The temperature obtained from the thermocouples on the substrate rear side revealed a measurable difference ($T_{S,1} \approx 125$ °C $< T_{S,2} \approx 135$ °C) indicating an elevated substrate temperature for condition 2. The difference observed was less pronounced than that recorded by the pyrometer, as the introduced heat must traverse the substrate. Both the substrate and the surface temperature revealed a measurable difference for both conditions. Those findings were in good agreement with the modeled thermal gradient at the impact zone (Ref 26), which was higher for condition 2 due to the higher temperature of impinging gas and particles. It can therefore be assumed that the hereby increased tensile stresses counteract the peening stresses and reduce the overall compressive stress level. However, the overall compressive stress level has not been shifted. Consequently, the additional heat input from condition 2 is insufficient to transition from general compressive toward tensile residual stresses. In order to achieve this state, it would be necessary either to increase the processing temperature of the gas further or to consider other factors like a shifted surface scanning speed or particle feed rate (Ref 24-26). However, this additional heat input was also evident in the results of the incremental hole drilling method for condition 2 in terms of reduced compressive residual stresses, where this effect was not superimposed by the geometric constraint of the cavity. It can thus be concluded that both methods provide reliable results in terms of relative difference for conditions 1 and 2. Consequently, it is possible to use the in situ curvature method as a fast and resource-saving method that does not require any complex sample preparation to make an initial estimate of the residual stresses in repair cavities as a result of the spray parameters. However, it should be noted that other (ex situ) methods are required for the final characterization of the anisotropic residual stresses in the cavity.

Conclusion

The use of cold gas spraying of IN718 in the context of component repair for filling up a 4 mm deep repair cavity was evaluated for two sets of parameters that differ in the gas temperature and pressure. Investigations were conducted on the topography, hardness, microstructure, and residual stresses of the resulting coating profile. The results of this study can be summarized as follows:

- The cold gas spray deposition of repair material demonstrated a certain sensitivity to the substrate geometry. The horizontally ordered cavity surface was filled completely. The deposition on a 60° wall angle resulted in a slightly lower deposition efficiency

and the deposition of surplus material in terms of slopes around the cavity surface.

- The microstructures of both conditions exhibited no significant differences, with an overall low porosity of less than 2%. Apparently, a satisfactory adhesion was achieved, even on the 60° tapered surfaces, which deviate from the optimum deposition angle. However, the assessment only bases on micrographs due to the lack of established adhesion tests on filled cavities.
- Vickers microhardness testing demonstrated a consistent hardness distribution within the repair filling and the substrate for both conditions, with comparable hardness values for both.
- The analysis of the incremental hole drilling method and the curvature method, conducted via ICP sensor, revealed that the compressive residual stresses were lower for condition 2. This was attributed to the particle impact at elevated temperatures and, in relation to this, lower velocity. The residual stress depth distributions determined by means of incremental hole drilling further indicate that the constraint of the elongated repair site has a clear impact on the residual stress state, which is clearly non-axisymmetric.
- This study demonstrates that the process parameters can be varied in a defined way to tailor the local residual stresses within the repair site of components made of IN718 with apparently only no significant changes in the microstructure and the adhesion of the repair coating.

Acknowledgment The authors acknowledge the financial support by the German Research Foundation (DFG) under grant numbers VA163/11-1 and GI376/18-1. Special thanks to Mr. Karl-Heinz Rauwald for his help to operate the cold spray facility.

Funding Open Access funding enabled and organized by Projekt DEAL.

References

1. M.B. Henderson, D. Arrell, R. Larsson, M. Heobel, and G. Marchant, Nickel Based Superalloy Welding Practices for Industrial Gas Turbine Applications, *Sci. Technol. Weld. Joining*, 2004, **9**(1), p 13-21.
2. T. Petrat, B. Graf, A. Gumenyuk, and M. Rethmeier, Laser Metal Deposition as Repair Technology for a Gas Turbine Burner Made of Inconel 718, *Phys. Procedia*, 2016, **83**, p 761-768.
3. O. Stier, Fundamental Cost Analysis of Cold Spray, *J. Therm. Spray Tech.*, 2014, **23**(1-2), p 131-139.
4. L.J. Kumar and C.G.K. Nair, Laser Metal Deposition Repair Applications for Inconel 718 Alloy, *Mater. Today: Proceed.*, 2017, **4**(10), p 11068-11077.
5. M. Grujicic, C.L. Zhao, W.S. DeRosset, and D. Helfritch, Adiabatic Shear Instability Based Mechanism for Particles/Substrate Bonding in the Cold-Gas Dynamic-Spray Process, *Mater. Des.*, 2004, **25**(8), p 681-688.
6. H. Assadi, F. Gärtner, T. Stoltenhoff, and H. Kreye, Bonding Mechanism in Cold Gas Spraying, *Acta Mater. Mater.*, 2003, **51**(15), p 4379-4394.
7. M. Faccoli, G. Cornacchia, D. Maestrini, G.P. Marconi, and R. Roberti, Cold Spray Repair of Martensitic Stainless Steel Components, *J. Therm. Spray Tech.*, 2014, **23**(8), p 1270-1280.
8. J.W. Murray, M.V. Zuccoli, and T. Hussain, Heat Treatment of Cold-Sprayed C355 Al for Repair: Microstructure and Mechanical Properties, *J. Therm. Spray Tech.*, 2018, **27**(1-2), p 159-168.
9. J. Fiebig, E. Bakan, T. Kalfhaus, G. Mauer, O. Guillon, and R. Vaßen, Thermal Spray Processes for the Repair of Gas Turbine Components, *Adv. Eng. Mater.*, 2020, **22**(6), p 1901237.
10. K. Ogawa and D. Seo, Repair of Turbine Blades Using Cold Spray Technique, *Advances in Gas Turbine Technology*. E. Benini Ed., InTech, 2011. p 499-526.
11. J.C. Lee, H.J. Kang, W.S. Chu, and S.H. Ahn, Repair of Damaged Mold Surface by Cold-Spray Method, *CIRP Ann.*, 2007, **56**(1), p 577-580.
12. B. Rottwinkel, C. Nölke, S. Kaierle, and V. Wesling, Crack Repair of Single Crystal Turbine Blades Using Laser Cladding Technology, *Procedia CIRP*, 2014, **22**, p 263-267.
13. R.N. Raoelison, Y. Xie, T. Sapanathan, M.P. Planche, R. Kromer, S. Costil, and C. Langlade, Cold Gas Dynamic Spray Technology: A Comprehensive Review of Processing Conditions for Various Technological Developments till to Date, *Addit. Manuf.. Manuf.*, 2018, **19**, p 134-159.
14. C. Cao, W. Li, Z. Zhang, X. Yang, and X. Yaxin, Cold Spray Additive Manufacturing of Ti6Al4V: Special Nozzle Design Using Numerical Simulation and Experimental Validation, *Coatings*, 2022, **12**(2), p 210.
15. S. Yin, P. Cavaliere, B. Aldwell, R. Jenkins, H. Liao, W. Li, and R. Lupoi, Cold Spray Additive Manufacturing and Repair: Fundamentals and Applications, *Addit. Manuf.. Manuf.*, 2018, **21**, p 628-650.
16. T. Suhonen, T. Varis, S. Dosta, M. Torrell, and J.M. Guilemany, Residual Stress Development in Cold Sprayed Al Cu and Ti Coatings, *Acta Mater. Mater.*, 2013, **61**(17), p 6329-6337.
17. T.W. Clyne and S.C. Gill, Residual Stresses in Thermal Spray Coatings and Their Effect on Interfacial Adhesion: A Review of Recent Work, *JTST*, 1996, **5**(4), p 401-418.
18. A. Vargas-Uscategui, P.C. King, M.J. Styles, M. Saleh, V. Luzin, and K. Thorogood, Residual Stresses in Cold Spray Additively Manufactured Hollow Titanium Cylinders, *J Therm Spray Tech*, 2020, **29**(6), p 1508-1524.
19. R. Vaßen, J. Fiebig, T. Kalfhaus, J. Gibmeier, A. Kostka, and S. Schrüfer, Correlation of Microstructure and Properties of Cold Gas Sprayed INCONEL 718 Coatings, *J Therm Spray Tech*, 2020, **29**(6), p 1455-1465.
20. R. Singh, S. Schruefer, S. Wilson, J. Gibmeier, and R. Vassen, Influence of Coating Thickness on Residual Stress and Adhesion-Strength of Cold-Sprayed Inconel 718 Coatings, *Surf. Coat. Technol.*, 2018, **350**, p 64-73.

21 F. Lang, J.-C. Schmitt, S. Cabeza, T. Pirling, J. Fiebig, R. Vassen, and J. Gibmeier, IN718 Cold Gas Repair Spray of Large Cavities—Microstructure and Residual Stresses, *Proceedings of the 10th International Symposium on Superalloy 718 and Derivatives*. E.A. Ott, J. Andersson, C. Sudbrack, Z. Bi, K. Bockenstedt, I. Dempster, M. Fahrmann, P. Jablonski, M. Kirka, X. Liu, D. Nagahama, T. Smith, M. Stockinger, A. Wessman Ed., Springer Nature Switzerland, Cham, 2023, p 739-753.
22. V. Luzin, K. Spencer, and M.-X. Zhang, Residual Stress and Thermo-Mechanical Properties of Cold Spray Metal Coatings, *Acta Mater. Mater.*, 2011, **59**(3), p 1259-1270.
23. G.G. Stoney, The Tension of Metallic Films Deposited by Electrolysis, *Proceedings of the Royal Society of London. Series A, Containing Papers of a Mathematical and Physical Character*, The Royal Society London, 1909, **82**(553), p 172-175.
24. D. Boruah, B. Ahmad, T.L. Lee, S. Kabra, A.K. Syed, P. McNutt, M. Doré, and X. Zhang, Evaluation of Residual Stresses Induced by Cold Spraying of Ti-6Al-4V on Ti-6Al-4V Substrates, *Surf. Coat. Technol.*, 2019, **374**, p 591-602.
25. S. Lett, A. Quet, S. Hémery, J. Cormier, E. Meillot, and P. Villechaise, Residual Stresses Development during Cold Spraying of Ti-6Al-4V Combined with In Situ Shot Peening, *J. Therm. Spray Tech.*, 2023, **32**, p 1018-1032.
26. J. Schmitt, J. Fiebig, S. Schrüfer, O. Guillon, and R. Vaßen, Adjusting Residual Stresses During Cold Spray Deposition of IN718, *J. Therm. Spray Tech.*, 2023, **33**, p 210-220.
27. J. Fiebig, J.-P. Gagnon, G. Mauer, E. Bakan, and R. Vaßen, In-Flight Measurements of Particle Temperature and Velocity with a High-Speed IR Camera During Cold Gas Spraying of In718 and TiAlCrNb, *J. Therm. Spray Tech.*, 2022, **31**(7), p 2013-2024.
28. A. Nastic and B. Jodoin, Evaluation of Heat Transfer Transport Coefficient for Cold Spray Through Computational Fluid Dynamics and Particle In-Flight Temperature Measurement Using a High-Speed IR Camera, *J. Therm. Spray Tech.*, 2018, **27**(8), p 1491-1517.
29. G. Mauer, R. Singh, K.-H. Rauwald, S. Schrüfer, S. Wilson, and R. Vaßen, Diagnostics of Cold-Sprayed Particle Velocities Approaching Critical Deposition Conditions, *J. Therm. Spray Tech.*, 2017, **26**(7), p 1423-1433.
30. R.G. Neo, W. Kaiqiang, S.C. Tan, and W. Zhou, Effect of Spray Distance and Powder Feed Rate on Particle Velocity in Cold Spray Processes, *Metals*, 2022, **12**(1), p 75.
31 H. Koivuluoto, J. Larjo, D. Marini, G. Pulci, and F. Marra, Cold-Sprayed Al6061 Coatings: Online Spray Monitoring and Influence of Process Parameters on Coating Properties, *Coatings*, 2020, **10**(4), p 348.
32. R. Singh, K.-H. Rauwald, E. Wessel, G. Mauer, S. Schruefer, A. Barth, S. Wilson, and R. Vassen, Effects of Substrate Roughness and Spray-Angle on Deposition Behavior of Cold-Sprayed Inconel 718, *Surf. Coat. Technol.*, 2017, **319**, p 249-259.
33. J. Pattison, S. Celotto, A. Khan, and W. O'Neill, Standoff Distance and Bow Shock Phenomena in the Cold Spray Process, *Surf. Coat. Technol.*, 2008, **202**(8), p 1443-1454.
34. W. Sun, A.W.Y. Tan, A. Bhowmik, I. Marinescu, X. Song, W. Zhai, F. Li, and E. Liu, Deposition Characteristics of Cold Sprayed Inconel 718 Particles on Inconel 718 Substrates with Different Surface Conditions, *Mater. Sci. Eng. A*, 2018, **720**, p 75-84.
35. "DIN EN ISO 6507-1:2024-01, Metallische Werkstoffe_- Härteprüfung Nach Vickers_- Teil_1: Prüfverfahren (ISO_6507-1:2023); Deutsche Fassung EN_ISO_6507-1:2023," Beuth Verlag GmbH, 2024.
36. J. Schindelin, I. Arganda-Carreras, E. Frise, V. Kaynig, M. Longair, T. Pietzsch, S. Preibisch, C. Rueden, S. Saalfeld, B. Schmid, J.-Y. Tinevez, D.J. White, V. Hartenstein, K. Eliceiri, P. Tomancak, and A. Cardona, Fiji: An Open-Source Platform for Biological-Image Analysis, *Nat. Methods*, 2012, **9**(7), p 676-682.
37. H. Koivuluoto, V. Matikainen, J. Larjo, and P. Vuoristo, Novel Online Diagnostic Analysis for In-Flight Particle Properties in Cold Spraying, *J Therm Spray Tech*, 2018, **27**(3), p 423-432.
38 G.S. Schajer, Measurement of Non-Uniform Residual Stresses Using the Hole-Drilling Method. Part II—Practical Application of the Integral Method, *J. Eng. Mater. Technol.*, 1988, **110**(4), p 344-349.
39. E. Obelode and J. Gibmeier, Residual Stress Analysis on Thick Film Systems by the Incremental Hole-Drilling Method - Simulation and Experimental Results, *Exp. Mech.*, 2013, **53**(6), p 965-976.
40. T. Schwarz and H. Kockelmann, Die Bohrlochmethode-Ein Für Viele Anwendungsbereiche Optimales Verfahren Zur Experimentellen Ermittlung von Eigenspannungen, *Messtechnische Briefe*, 1993, **29**(2), p 33-38.
41. E28 Committee, "Test Method for Determining Residual Stresses by the Hole-Drilling Strain-Gage Method," ASTM International, 2021.
42. T. Schwarz, "Beitrag Zur Eigenspannungsermittlung an Isotropen, Anisotropen Sowie Inhomogenen, Schichtweise Aufgebauten Werkstoffen Mittels Bohrlochmethode Und Ringkernverfahren," Staatliche Materialprüfungsanst. (MPA) Univ. Stuttgart, 1996.
43. E. Kröner, Berechnung der elastischen Konstanten des Vielkristalls aus den Konstanten des Einkristalls, *Z. Physik*, 1958, **151**(4), p 504-518.
44. D. Dye, S.M. Roberts, P.J. Withers, and R.C. Reed, The Determination of the Residual Strains and Stresses in a Tungsten Inert Gas Welded Sheet of IN718 Superalloy Using Neutron Diffraction, *The J. Strain Anal. Eng. Design*, 2000, **35**(4), p 247-259.
45. M.G. Mutter, *"Herstellung thermisch gespritzter Schichten mit optimierten Spannungseigenschaften", (Jülich)*, Zentralbibliothek, Verlag, Forschungszentrum Jülich GmbH, 2016.
46. F. Oviedo and A. Valarezo, Residual Stress in High-Velocity Impact Coatings: Parametric Finite Element Analysis Approach, *J. Therm. Spray Tech.*, 2020, **29**(6), p 1268-1288.